Unraveling the Dynamic Network in the Reactions of an Alkyl Aryl Ether Catalyzed by Ni/ γ -Al₂O₃ in 2-Propanol

Long Qi,^{1,2,3} Ali Chamas,¹ Zachary R. Jones,¹ Eric D. Walter,⁴ David W. Hoyt,⁴ Nancy M. Washton,⁴ Susannah L. Scott^{1,2*}

KEYWORDS Interfacial Reactions, Reaction Network, C-O Bond Hydrogenolysis, Solvent Effect, Arene Hydrogenation, C-H Activation, Induction Period, Operando NMR Spectroscopy

ABSTRACT: The reductive cleavage of aryl ether linkages is a key step in the disassembly of lignin to its monolignol components, where selectivity is determined by the kinetics of multiple parallel and consecutive liquid-phase reactions. Triphasic hydrogenolysis of 13 C-labeled benzyl phenyl ether (BPE, a model compound with the same C-O bond energy as the major β-O-4 linkage in lignin), catalyzed by Ni/γ-Al₂O₃, was observed directly at elevated temperatures (150 - 175 °C) and pressures (79-89 bar) using *operando* magic-angle spinning NMR spectroscopy. Liquid-vapor partitioning in the NMR rotor was quantified using the 13 C NMR resonances for the 2-propanol solvent, whose chemical shifts report on the internal reactor temperature. At 170 °C, BPE is converted to toluene and phenol with $k_1 = 0.17 \text{ s}^{-1} \text{ g}_{cat}^{-1}$, and an apparent activation barrier of (80 ± 8) kJ mol⁻¹. Subsequent phenol hydrogenation occurs much more slowly ($k_2 = 0.0052 \text{ s}^{-1} \text{ g}_{cat}^{-1}$ at 170-175 °C), such that cyclohexanol formation is significant only at higher temperatures. Toluene is stable under these reaction conditions, but its methyl group undergoes facile H/D exchange ($k_3 = 0.046 \text{ s}^{-1} \text{ g}_{cat}^{-1}$ at 175 °C). While the source of the reducing equivalents for both hydrogenolysis and hydrogenation is exclusively H₂/D_{2(g)} rather than the alcohol solvent at these temperatures, the initial isotopic composition of adsorbed H/D on the catalyst surface is principally determined by the solvent isotopic composition (2-PrOH/D). All reactions are preceded by a pronounced induction period associated with catalyst activation. In air, Ni nanoparticles are passivated by a surface oxide monolayer, whose removal under H₂ proceeds with an apparent activation barrier of (72 ± 13) kJ mol⁻¹. The *operando* NMR spectra provide molecularly-specific, time-resolved information about the multiple simultaneous and sequential processes as they occur at the solid-liquid interface.

INTRODUCTION

Liquid-phase reactions catalyzed by supported metals are important in the upgrading of low volatility chemical feedstocks, notably those obtained from renewable biomass. The presence of water, organic co-solvents, reactive solutes and spectator species, including ions, represent significant challenges for understanding and predicting reactions that occur at or near solid-liquid interfaces, especially when the conditions involve elevated temperatures and pressures.1 For example, the reductive depolymerization of lignin which liberates aromatic monomers via hydrogenolysis of the aryl ether C-O linkages typically takes place in a triphasic solid-liquid-gas mixture at T > 100 °C and P > 10 bar. Although computational studies can provide valuable guidance regarding the possible behaviors of various functional groups on well-defined metal surfaces, 7-12 they generally do not account for the complex reaction networks and realistic reaction conditions involved in the catalytic depolymerization of lignin. Most experimental studies have been conducted using compositional analysis of quenched reaction mixtures,4 which often suffer from poor mass balance, and generate few kinetic or mechanistic insights.13

Since the C-O bond strength in benzyl phenyl ether (BPE) is

predicted ¹⁴ to be comparable to that of the major β -O-4 aryl ether C-O linkages in lignin, 15 BPE has been widely used as a simple model for the biopolymer in studies of the kinetics and mechanism of C-O bond cleavage and subsequent reactions (although the presence of hydroxy and/or methoxy substitutents may alter actual rates appreciably). Reaction occurs at the Ar-O bond for diaryl and simple alkyl aryl ethers, but switches to the Bn-O bond for aryl benzyl ethers such as BPE, 16-18 as well as in in lignin itself. The hydrogenolysis of simple ethers and lignin ether bonds is catalyzed by a variety of soluble and solid phase catalysts. 19 In this work, we investigated Nicatalyzed BPE hydrogenolysis via operando NMR experiments performed at elevated temperatures/pressures in magic-angle spinning (MAS) rotors capable of acquiring high-resolution spectra for three-phase mixtures (solid, liquid, and gas). The expected reactions are hydrogenolysis and competing hydrogenation, Scheme 1.

Highly dispersed Cu or Pd catalysts are well-established for use in hydrogenolysis reactions, ²⁰⁻²¹ but Ni-based catalysts have emerged recently as interesting substitutes. Ni is more Earth-abundant than Pd, and it activates H₂ more readily than Cu. ²²⁻²⁵ However, unlike Pd and Cu, Ni nanoparticles more readily undergo surface oxidation, which results in their passivation upon exposure to air. ²⁶⁻²⁸ When a

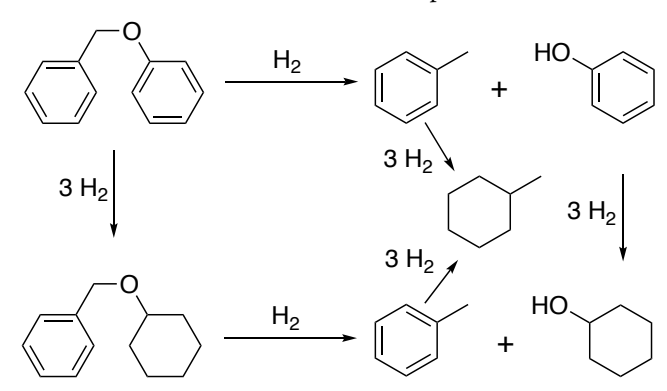
¹Department of Chemistry & Biochemistry, University of California, Santa Barbara, California 93106, USA.

²Department of Chemical Engineering, University of California, Santa Barbara, California 93106, USA.

³ U.S. DOE Ames Laboratory, Iowa State University, Ames, Iowa 50011, USA.

⁴ Environmental Molecular Sciences Laboratory, Pacific Northwest National Laboratory, Richland, WA 99354, USA.

Ni catalyst is activated *in situ*, the need to remove overlayers on the catalyst surface, catalyst restructuring, and/or the formation of active sites can lead to substantial induction periods.²⁹⁻³¹



Scheme 1. Possible reactions in benzyl phenyl ether (BPE) hydrogenolysis to toluene and phenol, with competing aromatic hydrogenation.

Unfortunately, kinetic and mechanistic information inferred from yields measured at extended times convolute the rate of activation with the kinetics of subsequent catalytic reactions. In this study, high-quality *operando* NMR data combined with isotopic labeling provide details on the kinetics and mechanism of Ni/ γ -Al₂O₃ activation, the length of the induction period and the nature of its termination, the activity of the catalyst towards each of the organic components in solution as a function of the extent of reaction, the participation of the solvent, and the dynamic network of H/D exchange reactions that accompany catalytic ether hydrogenolysis.

RESULTS AND DISCUSSION

Design of the *Operando* **NMR Study.** Recently, we demonstrated the use of sealed MAS NMR rotors in reactions conducted in near-supercritical 2-PrOH (225 °C, P = 200 bar). ³²⁻³³ At room temperature, the ¹³C MAS-NMR spectrum of 2-PrOH consists of two singlets at δ 25.3 (methyl) and 63.6 (methine) ppm, Figure 1. As the temperature of the sealed NMR rotor approaches 150 °C, the methyl and methine resonances shift to lower and higher frequencies, respectively, while two new resonances emerge at δ 23.2 and 63.1 ppm. The intensities of the latter increase with temperature, at the expense of the original 2-PrOH resonances. The positions of the new resonances also shift gradually to higher frequencies as the temperature rises.

The position of the new resonances is not consistent with a chemical reaction (e.g., the condensation of 2-PrOH to form diisopropyl ether). Furthermore, their appearance is readily reversible: when the rotor is cooled to room temperature, the intensities decrease and the resonances vanish. On this basis, we assign the new resonances to 2-PrOH vapor. Their intensities are consistent with the saturation vapor pressure of 2-PrOH (e.g., at 150 °C, the solvent is 5.5 % vaporized, corresponding to a pressure of ca. 10 bar, compared to the saturation vapor pressure of 9 bar at this temperature). The lower frequencies of both vapor-phase resonances relative to the corresponding liquid-phase resonances are consistent with reduced intermolecular interactions, such as Hbonding, which are generally deshielding.³⁴ Three of the four 2-PrOH resonances shift linearly with temperature, Figure S1. The chemical shift of the methine resonance of liquid 2-PrOH is an exception, exhibiting slightly non-monotonic behavior.

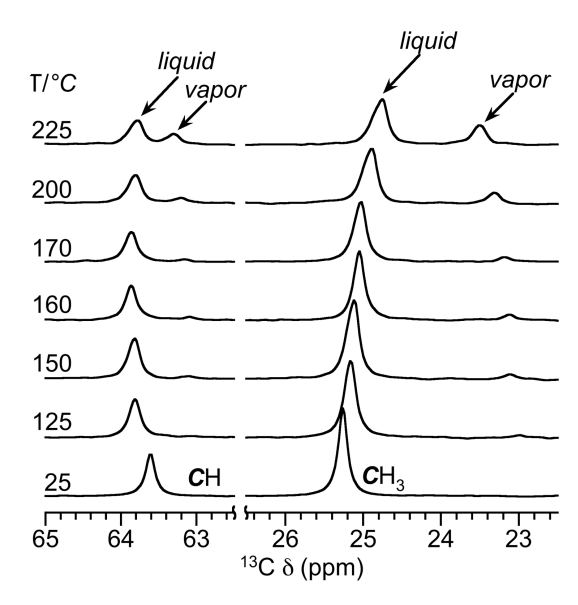
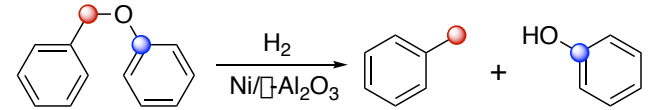


Figure 1. Variable temperature direct polarization ^{13}C MAS-NMR spectra of 2-PrOH, recorded in a sealed rotor, and showing distinct resonances for liquid and vapor phase species. The 5-mm o.d. NMR rotor (internal volume 140 μ L) was charged with 40 μ L 2-PrOH and 50 bar H_2 at room temperature. The estimated total internal pressure, including the saturated vapor pressure of 2-PrOH, rises from 71 bar at 125 °C to 118 bar at 225 °C. Each spectrum represents 32 scans with a recycle delay of 60 s and line broadening of 15 Hz. MAS rate: 5 kHz.

Usually, the temperature in solid-state NMR experiments must be estimated using an external thermal reference, such as ²⁰⁷Pb(NO₃)₂.³⁵⁻³⁶ Here, direct observation of temperaturedependent chemical shifts for the solvent, and its vapor-liquid equilibrium, allow us to measure the internal temperature of the NMR rotor and to assess its thermal stability during operando experiments. Using the intensity ratios of 2-PrOH liquid and vapor phase resonances, we estimate the time required for the internal rotor temperature to stabilize after the probe temperature reaches 150 °C to be ≤14 min. During this time, the rotor temperature rises ca. 5 °C, as judged by the 0.02 ppm change in chemical shift for the methyl resonance of 2-PrOH. Subsequent thermal drift, which would change the liquid:vapor ratio, was not detected. The integrity of the rotor seals is also readily assessed. A leak would cause the area of the liquid resonance to decrease continuously, while the area of the corresponding vapor resonance would grow initially as the liquid volume shrinks. The constant combined areas of liquid and vapor peaks in the spectra in Figure 1 confirm that the NMR rotor lost no material during the course of the experiment. The spectra are unchanged in the presence of $H_{2(g)}$.

Partial solvent vaporization causes the liquid-phase concentrations of non-volatile components in the NMR rotor to vary significantly with temperature. The extent of vaporization is readily quantified by integration of the internal solvent resonances. In the experiment shown in Figure 1, (6.1 ± 0.8) % of the 2-PrOH was present in the vapor phase at 150 °C, rising to (30.1 ± 1.5) % at 225 °C. Taking both solvent vaporization and liquid expansion into account, a dissolved solute will experience an increase in concentration of 6.5 % at 150 °C, and 43 % at 225 °C, relative to its initial concentration at room temperature. These concentration changes have significant implications for non-first-order reaction kinetics.

Catalytic Hydrogenolysis of Benzyl Phenyl Ether (BPE). To enhance sensitivity in the NMR experiments, BPE was selectively ^{13}C -labeled as shown in Scheme 2. In 2-PrOH at room temperature, the ^{13}C MAS-NMR spectrum consists of two singlets at δ 70.1 and 159.3 ppm, corresponding to the methylene and phenolate-C1 carbons, respectively. The appearance of the spectrum was unchanged in the presence of either γ -Al₂O₃ or Ni/ γ -Al₂O₃ (2 wt% Ni), Figure S2, therefore the presence of superparamagnetic 37 Ni nanoparticles does not impede the detection of organic molecules in the solution phase. The concentrations of species adsorbed on the catalyst surface are presumably below the detection limit.



Scheme 2. Benzyl phenyl ether (BPE, selectively 13 C-labeled at the benzylic (red, BPE-B) and phenolate- C_1 (blue, BPE-P) positions. Hydrogenolysis results in toluene- α - 13 C and phenol- 13 C.

After standing for 3 d at 25 °C under 50 bar H₂, there were no changes in the ¹³C MAS-NMR spectrum. However, when the rotor was heated to 150 °C, a reaction was detected within the first hour. A typical array of NMR spectra is shown in Figure 2. The two BPE ¹³C resonances began to disappear after an initial induction period. The onset of BPE conversion coincides with the appearance of phenol-1- 13 C and toluene- α - 13 C resonances, which appear as singlets at δ 157.8 and 20.8 ppm, respectively. At the end of the reaction, the selectivities for both products exceeds 95 %. These values include the contribution at δ 18.3 ppm for toluene vapor (which disappeared when the rotor was cooled to room temperature). No vapor phase peaks for BPE or phenol were detected at any of the temperatures in this study, due to their lower volatilities. Since no benzene was detected (ca. 128.4 ppm), hydrogenolytic cleavage of BPE occurs selectively at the Bn-O bond, as expected owing to its lower bond dissociation energy relative to the Ph-O bond. 38-39

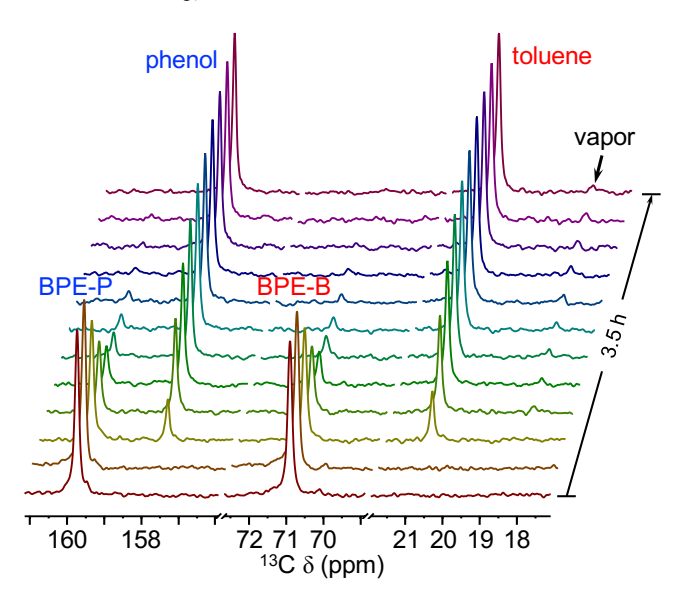


Figure 2. Operando array of direct polarization ¹³C MAS-NMR spectra recorded during BPE hydrogenolysis at 150 °C, showing conversion of BPE to toluene- α -¹³C and phenol-¹³C₁. The ¹³C-labeled positions of BPE are indicated as BPE-B (benzylic) and BPE-P (phenolate-C₁). The rotor was initially loaded with 2 wt% Ni/γ-

Al₂O₃ (10 mg, air exposed), BPE (2.0 mg, 0.011 mmol), and 2-PrOH (40 μ L, 0.52 mmol), and pressurized with 50 bar H₂ (0.20 mmol) at room temperature (giving a H₂ pressure of 70 bar and 2-PrOH pressure of 9 bar, for a total pressure of 79 bar at 150 °C). MAS rate: 5 kHz.

No hydrogenation of either BPE or toluene was observed, although some hydrogenation of toluene was seen previously at a higher temperature and pressure (225 °C, 120 bar H_2).³² However, phenol is more reactive, ¹³ and it was partially hydrogenated to cyclohexanol (ca. 3 % conversion in 10 h at 150 °C, Figure S3).

Kinetics of BPE Hydrogenolysis. Kinetic profiles extracted from time-resolved operando 13C MAS-NMR spectra are shown in Figure 3. The extended induction period is attributed to catalyst activation, which lasts slightly longer than the thermal equilibration period of the NMR rotor (≤ 14 min at 150 °C). This temporal separation between catalyst activation and BPE conversion is fortuitous, since it ensures the collection of isothermal kinetic data during the hydrogenolysis reaction. Reaction profiles were truncated to eliminate measurements made during the induction period prior to kinetic analysis (however, we note that this approach is not justified when there is significant temporal overlap of the kinetic phases). The remaining data were analyzed with a first-order rate equation, to give the curvefits shown in Figure 3. All four pseudo-first-order rate constants $(k_{1,obs})$ extracted from data for each of the four observed ¹³C resonances (i.e., BPE-B, BPE-P, toluene-C_α, and phenol-1-C) are very similar, with an average value of (0.56 ± 0.04) x 10⁻³ s⁻¹ at 150 °C (Table 1).

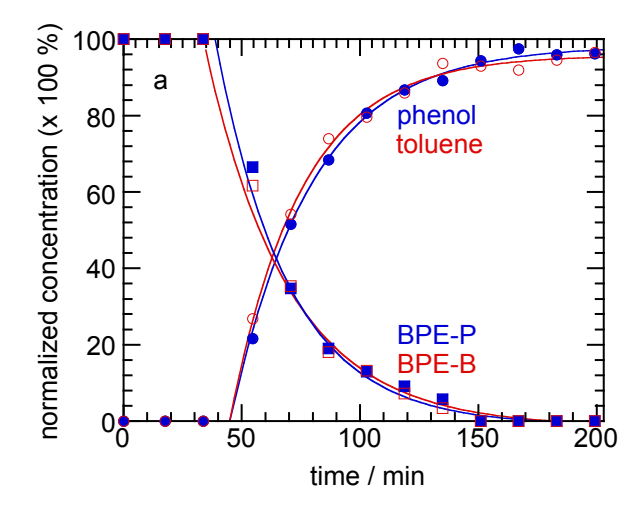


Figure 3. Kinetic profiles for BPE hydrogenolysis to toluene and phenol, in a rotor loaded with air-exposed 2 wt% Ni/ γ -Al₂O₃ in 2-PrOH and 50 bar H₂ (giving a total pressure of 79 bar at 150 °C), based on resonance intensities normalized to the initial BPE concentration, for the two BPE resonances (squares) and its two primary hydrogenolysis products (circles). Data recording started when the NMR probe reached 150 °C. The curvefits (solid lines) were obtained by fitting the first-order rate equation to the portion of the data remaining after removal of measurements made during the initial induction period.

The dependence of $k_{\rm obs}$ on $P({\rm H_2})$ is weak, as shown by kinetic profiles recorded in rotors charged with initial ${\rm H_2}$ pressures of $50 \le P({\rm H_2}) \le 125$ bar (Figure S4), consistent with previous work.⁴⁰ In the $^1{\rm H}$ MAS-NMR spectrum, ${\rm H_2}_{(g)}$ appears as a singlet at δ 4.2 ppm

Table 1. Temperature-dependence of pseudo-first-order rate constants and kinetic isotope effects for BPE hydrogenolysis catalyzed by Ni/ γ -Al₂O₃ in 2-propanol

Exp	T	Catalyst mass	Solvent ^a	Gas	$D/(H+D)^b$	10 ³ k _{1,obs} (s ⁻¹) ^c					
	°C	mg			%	BPE-B	BPE-P	BPE (avg)	Toluene	Phenol	Phenol+Cyclohexanol
1	150	9.8	2-PrOH	H_2	0	0.59(2)	0.60(3)	0.60(2)	0.54(2)	0.50(2)	n.a.
2	160	10.0	2-PrOH	H_2	0	1.16(15)	1.17(12)	1.16(14)	0.91(10)	1.12(51)	n.a.
3	170	10.1	2-PrOH	H_2	0	1.63(8)	1.70(10)	1.66(8)	1.37(21)	1.10(14)	n.a.
4	175	10.1	2-PrOD	D_2	100	1.51(14)	1.28(16)	1.38(15)	1.43(14)	$1.00(7)^{d}$	1.55(18)
5	175	10.0	2-PrOH	D_2	43	1.82(13)	1.73(16)	1.78(14)	1.62(17)	$1.18(10)^{d}$	1.49(11)
6	175	10.1	2-PrOD	H_2	57	1.10(6)	0.95(5)	1.03(5)	0.96(7)	$0.61(4)^{d}$	0.79(8)

^a 2-PrOH is (CH₃)₂CHOH; 2-PrOD is (CD₃)₂CDOD. ^b Fractional abundance (%) of exchangeable H/D atoms, contributed by H₂/D₂ (two atoms per molecule) and 2-PrOH/D (one atom per molecule). ^c Except where noted, all rate constants were obtained from non-linear least-squares fits of the first-order rate equation to concentration profiles obtained in *operando* MAS-NMR experiments, after data truncation to remove the induction period. Values in parentheses represent non-linear least-squares curvefit errors. ^d Obtained from a non-linear least-squares fit of a biexponential rate equation ⁴⁴ to the concentration profile, to account for sequential ether hydrogenolysis and hydrogenation of phenol to cyclohexanol. n.a. = not applicable (because the yield of cyclohexanol was negligible).

while dissolved H_2 is a singlet at δ 4.6 ppm, $^{41-42}$ Figure S5. Since it was initially present in ca. 20-fold excess relative to BPE, the change in H_2 concentration over the course of the reaction is small. Indeed, the intensities of the 4.2 and 4.6 ppm resonances, measured at 25 °C before and after reaction, decreased negligibly. Temperature effects on H_2 solubility are reported to be weak in the temperature range of interest. However, the concentration of dissolved H_2 increased slightly, from 0.35 M at 150 °C to 0.47 M at 170 °C, due to the increase in pressure.

To ensure that environmental conditions specific to the NMR rotor (such as magic-angle spinning) do not influence the kinetics, and that mass transport limitations do not affect the rate, the reaction was also conducted in a 25 mL batch reactor at 150 °C using the same BPE concentration, catalyst:BPE ratio, solvent, and $P(H_2)$. The reaction progress was monitored by exsitu GC analysis of liquid aliquots removed at timed intervals. A short induction period (ca. 10 min) was observed when air-exposed Ni/ γ -Al₂O₃ (2 wt%) was used as the catalyst, Figure S6. Both BPE conversion and toluene formation are pseudo-first-order. Despite the lower time resolution of the batch reactor experiment, the observed rate constants are comparable to those obtained by the *operando* NMR method.

Similar NMR experiments conducted at 160 and 170 °C are shown in Figure 4a. Because $k_{\rm l,obs}$ does not depend on the concentration of BPE (the limiting reagent), the pseudo-first-order rate constants are not affected by temperature-dependent changes in the extent of solvent vaporization. At the highest reaction temperature, the rate of phenol formation is slower than that of toluene (Table 1). However, this effect disappears when the combined rate of formation of phenol and cyclohexanol is analyzed.

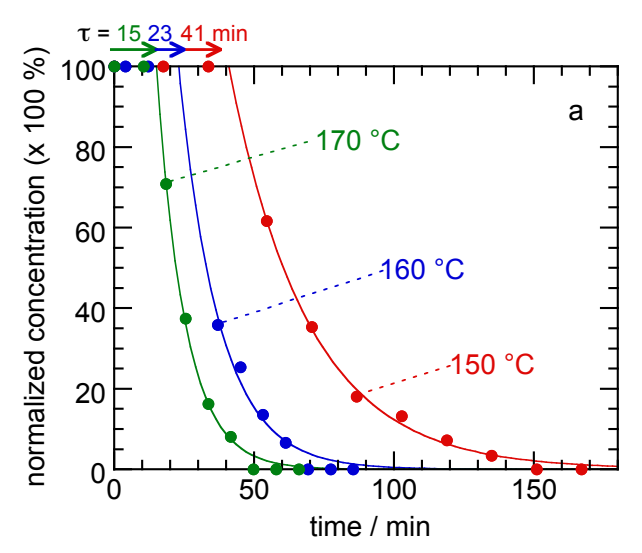
Pseudo-first-order rate constants were normalized by dividing the average $k_{\rm obs}$ value measured for BPE conversion (i.e., the mean of values obtained using the data from the BPE-B and BPE-P resonances) by the catalyst mass, and the normalized rate constants were used to construct the Arrhenius plot in Figure 4b. The apparent activation energy (including adsorption/desorption energies and intrinsic reaction barriers) for BPE hydrogenolysis in 2-PrOH is (80 \pm 8) kJ mol⁻¹. This value is essentially the same as a previous report, 72 kJ mol⁻¹ (no error reported), for the same reaction catalyzed by silica-supported Ni nanoparticles suspended in water. ⁴⁰ It is a small

but significant fraction of the calculated Bn-O bond dissociation energy (236 kJ mol $^{-1}$), ¹⁴ which DFT calculations suggest is the rate-determining step. ⁴⁵

H/D Isotopic Exchange during Aryl Ether Hydrogenolysis.

The small volume of the solid-state NMR rotor facilitates the use of isotopically-labeled gases and solvents in mechanistic studies. When the reaction of BPE was conducted with D_2 in 2-PrOH at 175 °C, a new 13 C NMR resonance at δ 63.8 ppm (assigned to a methine resonance of 2-PrOH) was detected near the end of the induction period, just before the appearance of toluene (Figure S7). Initially, it emerged as a low frequency shoulder on the original solvent methine resonance (δ 64.0 ppm), then grew in at the expense of that peak.

H/D exchange in the methine group of 2-PrOH can be ruled out, since such exchange would give rise to a 1:1:1 triplet characteristic of C-D coupling. This result also shows that solvent is not serving as a significant source of H_2 under the reaction conditions, since its dehydrogenation-rehydrogenation would result in such isotopic exchange at the methine C-H bond, Scheme 3a. Furthermore, the spectra show no evidence for H/D exchange in the CH_3 groups of



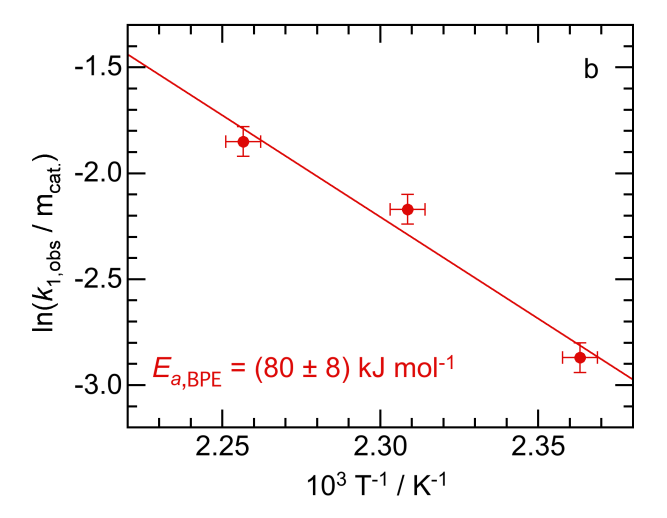


Figure 4. (a) Variable temperature reaction profiles for hydrogenolysis of BPE (2.0 mg, 0.011 mmol) in 2-PrOH (40 μ L, 0.52 mmol) with 50 bar H₂ (0.20 mmol) catalyzed by Ni/ γ -Al₂O₃ (2 wt% Ni, ca. 10 mg, air-exposed). Total internal pressures at 150-170 °C were estimated to be 79-86 bar. Curvefits (lines) were obtained using a first-order rate law, after truncation to remove data recorded during the induction period (see Table 1 for rate constants). The length of the induction period (τ) was estimated by extrapolating the first-order kinetic curvefit to 0% conversion. (b) Arrhenius plot of pseudo-first-order rate constants for BPE hydrogenolysis (normalized by catalyst mass; the uncertainty reflects full error propagation in the Arrhenius equation, 47 not the error in the linear fit parameters).

Scheme 3. Three possible routes for H/D exchange in 2-PrOH, catalyzed by Ni/ γ -Al₂O₃. Only route (c) was detected experimentally for temperatures \leq 175 °C.

2-propanol (as would be expected from alcohol dehydration-rehydration), Scheme 3b. Aluminas are known to catalyze 2-propanol dehydration in the gas phase, but at higher temperatures (> $200\,^{\circ}\text{C}$). A blank experiment conducted at 175 °C with BPE in the presence of 2-PrOH and the alumina support (i.e., no Ni or H₂). After 12 h, there was no conversion of BPE, and no ^{13}C NMR peaks for either diisopropyl ether (dehydration product) or acetone (dehydration product).

Definitive assignment of the new 13 C NMR resonance at 63.8 ppm to $(CH_3)_2CHO\boldsymbol{D}$ was achieved by comparison to the solution-state 13 C NMR spectrum of an equimolar mixture of $(CH_3)_2CHO\boldsymbol{D}$ and $(CH_3)_2CHO\boldsymbol{H}$, Figure S8. The methine 13 C chemical shifts of these isotopologs differ by only 15.2 Hz, mostly likely due to slight differences in intermolecular interactions. The difference in the methyl 13 C chemical shifts caused by OH/OD exchange is even smaller (6.8 Hz), and is not visible in the MAS-NMR spectra.

Thus 2-PrOH undergoes slow exchange with D_2 *only* at its hydroxyl group, Scheme 3c. A kinetic profile for this reaction, catalyzed by Ni/ γ -Al₂O₃, is shown in Figure S9. The pronounced induction period (40 min at 175 °C) suggests that exchange is catalyzed by the activated (i.e., reduced) form of the catalyst (*vide infra*). The final conversion to (CH₃)₂CHO**D**, 44 %, is essentially the same as the initial fraction of exchangeable deuterium D/(D+H), 43 %, present in the 2-PrO<u>H</u>/ \underline{D}_2 mixture.

The effect of isotopic substitution in either the solvent or the gas (H_2/D_2) on the rate of the principal reaction, BPE cleavage, is minor, Table 1. The apparent kinetic isotope effect (KIE), $k_{\rm l,H}/k_{\rm l,D}$ = (1.3 ± 0.2), is the ratio of the average rate constants obtained using the two BPE signals in Expts 3 and 4 (note that the reaction temperatures are slightly different, but the higher temperature in Expt 4 with D_2 will attenuate, not enhance, the rate difference). A small (i.e., secondary) KIE value is consistent with rate-determining C-O bond cleavage.

Phenol Hydrogenation. Formation of cyclohexanol becomes significant only at $T \ge 170$ °C, as shown by the appearance of a singlet at δ 69.7 ppm for cyclohexanol-1-¹³C. In principle, cyclohexanol could be formed via partial hydrogenation of BPE to give benzyl cyclohexyl ether followed by C-O bond cleavage, or directly by phenol hydrogenation (Scheme 1). However, no ¹³C NMR signals were detected for benzyl cyclohexyl ether. Furthermore, the rate of disappearance of the BPE-P signal is the same as that of the BPE-B signal (Table 1). Consequently, we can confidently infer that cyclohexanol is formed via phenol hydrogenation.

Cyclohexanol can undergo reversible acid-catalyzed dehydration to cyclohexene, which would cause the $^{13}\mathrm{C}$ label to be distributed over all six cyclohexanol carbons. This scrambling would reduce the intensity of the cyclohexanol-1- $^{13}\mathrm{C}$ resonance over time, and lead to the appearance of several new cyclohexanol resonances (δ 34.7, 25.1, and 23.7 ppm). Since this effect was not observed, cyclohexanol dehydration (as well as 2-PrOH dehydration) is not significant under the reaction conditions. We can also rule out rapid hydrogenation of cyclohexene to cyclohexane, since the latter was not detected either, although cyclohexane was observed in our previous study conducted at a higher reaction temperature.

The kinetic profile for phenol shown in Figure 5 has the typical biexponential shape of a reaction intermediate. The curve was analyzed using two pseudo-first-order rate constants. Kinetic ambiguity precludes *a priori* assignment of the rate constants.⁴⁴ However, the larger value is similar to the $k_{1,\text{obs}}$ value obtained from single exponential fit to the BPE profiles (Table 1), and is therefore attributed to BPE hydrogenolysis. We attribute the smaller of the two values, $k_{2,\text{obs}} = (5.2 \pm 0.4) \times 10^{-5} \text{ s}^{-1}$, to phenol hydrogenation. This value corresponds to $k_2 = (5.2 \pm 0.4) \times 10^{-3} \text{ s}^{-1} \text{ g}_{\text{cat}}^{-1}$ at 175 °C, making phenol conversion to cyclohexanol ca. 30x slower than C-O bond cleavage under the reaction conditions.

When BPE hydrogenolysis was conducted in the presence of readily-exchangeable deuterium (present either in the solvent, as 2-PrOD, or in the gas, as D₂), a new cyclohexanol resonance appeared adjacent to the singlet at δ 69.7 ppm (Figure S10). The signal, at δ 69.2 ppm (t, 1:1:1, ${}^1J_{C-D}$ = 21.5 Hz), reflects H/D exchange at the C₁ position, Scheme 4. Presumably, D is also incorporated at other ring positions during phenol hydrogenation, but the effect is not detectable because the other ring carbons do not become ${}^{13}C$ -labeled. The hydroxyl protons of both phenol and cyclohexanol are

also expected to undergo rapid H/D exchange in the presence of exchangeable deuterium.

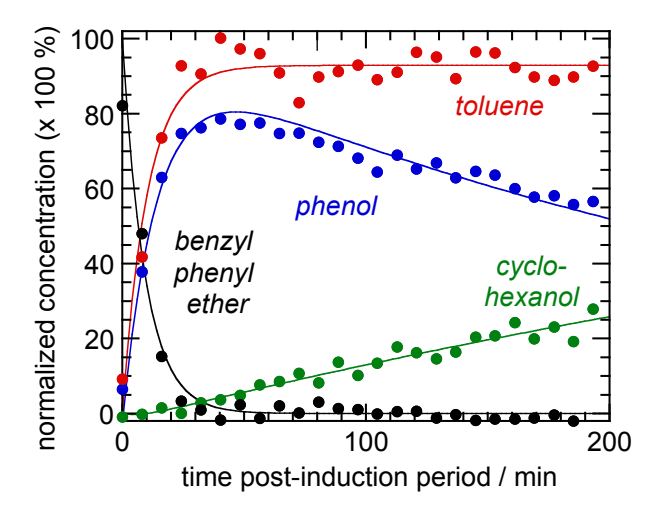
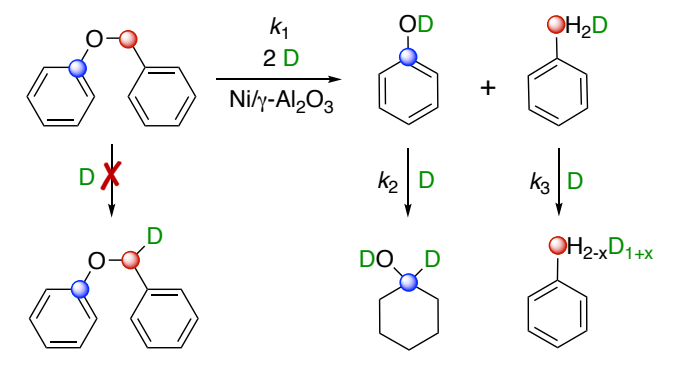


Figure 5. Kinetic analysis of individual 13 C NMR profiles recorded during BPE conversion in a rotor loaded with air-exposed Ni/γ-Al₂O₃ (2 wt%) and 50 bar D₂ in 2-PrOH, after heating to 175 °C (resulting in a total pressure of 89 bar). Data collected during the induction period were removed prior to non-linear least-squares curvefitting. The BPE and toluene profiles were analyzed with a single exponential rate equation; the phenol and cyclohexanol profiles were analyzed with a biexponential rate equation.

When BPE cleavage was performed in 2-PrOH in the presence of D₂, no KIE for phenol ring saturation was observed. However, conducting the reaction in 2-PrOD in the presence of H₂ resulted in an inverse kinetic isotope effect of $k_{2,H}/k_{2,D} = (0.66 \pm 0.14)$. In these experiments, the total amounts of exchangeable D contributed by the gas and the solvent were comparable. Inverse KIEs of 0.5 - 0.8



Scheme 4. Deuterium incorporation into 13 C-labeled BPE and its reaction products, in the presence of D_2 and/or 2-PrOD.

have been reported for ring saturation of benzene and simple alkylaromatics, where they arise due to the $\rm sp^2$ -to- $\rm sp^3$ rehybridization of ring carbons. ⁴⁹⁻⁵² Comparing the reaction rates in either 2-PrOH with $\rm D_{2(g)}$, or in 2-PrOD with $\rm H_{2(g)}$, revealed that the kinetics of phenol saturation is influenced primarily by the isotopic composition of the solvent. The solvent kinetic isotope effect is unexpected, considering that the experiments described above showed the reducing agent to be exclusively $\rm H_2/\rm D_{2(g)}$, not 2-propanol. It suggests that the catalyst activates only a small fraction of the available $\rm H_2/\rm D_{2(g)}$ at a given time, and that exchange between

adsorbed H/D and $H_2/D_{2(g)}$ is slow relative to exchange between adsorbed atomic H/D and 2-PrOH/D.

The H/D exchange reaction on the surface of the catalyst is shown in eq 1, where H^*/D^* represents the adsorbed H/D.

$$H^* + 2\text{-PrOD} \leftrightarrows D^* + 2\text{-PrOH} \tag{1}$$

From the Ni(0) dispersion, we estimate the maximum amount of adsorbed H/D to be ca. 0.06 %, relative to the exchangeable H/D initially present as H_2/D_2 in the rotor. In the early stages of phenol hydrogenation, the isotopic composition of adsorbed H/D will therefore be determined principally by the isotopic composition of the solvent (2-PrOH/D), assuming that exchange is fast between adsorbed H/D and the solvent. Based on the conversion of 2-PrOH to 2-PrOD in the presence of D_2 , measured by observing the formation of the new 13 C resonance for 2-PrOD at 63.8 ppm, the exchange rate constant was estimated to be $(0.044 \pm 0.008) \, \text{s}^{-1} \, \text{g}_{\text{cat}}^{-1}$ at 175 °C (Figure S9). At longer reaction times, when extensive H/D exchange between gas and solvent has occurred, the effect on k_2 is minor, since phenol hydrogenation is already largely complete.

H/D Isotopic Exchange in Toluene. No methylcyclohexane was detected in any experiment, although our previous study reported slow catalytic hydrogenation of toluene at a higher reaction temperature, 225 °C. ³² However, when BPE cleavage was conducted in 2-PrOD at 175 °C, the appearance of the expected singlet at 20.6 ppm for the toluene methyl group was accompanied by several new peaks at slightly lower frequencies, Figure 6a. The peaks show the characteristic ¹³C-D coupling patterns of partially deuterated methyl groups, Figure 6b. The chemical shifts for each toluene isotopolog, extracted from these spectra, are shown in Table S3. D incorporation into toluene was also confirmed by MS analysis, Figure S11.

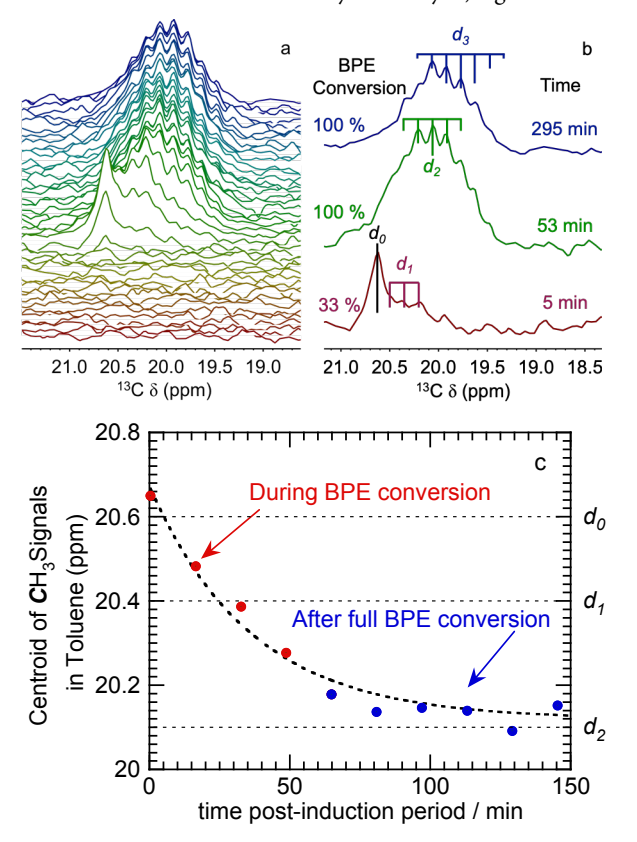


Figure 6. Formation of toluene- α - d_n during BPE hydrogenolysis in a rotor loaded with Ni/ γ -Al₂O₃ (10.0 mg, 2 wt% Ni) in 2-PrOD and

50 bar H_2 and heated to 175 °C (resulting in a total pressure of 89 bar, and a ratio of exchangeable D/(H+D) = 0.57): (a) time-resolved array of *operando* ¹³C MAS-NMR spectra, showing the evolution of the ¹³CH_{3-x}D_x resonances; (b) comparison of characteristic ¹³C-²H coupling patterns with ¹³C resonances observed 5 min after the end of induction period (at 33 % BPE conversion), 48 min later (at 100 % BPE conversion), and at the end of the experiment; (c) time evolution of the centroid for the ¹³CH_{3-x}D_x resonance (points), with a single exponential curvefit for H/D exchange (bold dashed line), and indicators for the chemical shifts for the various toluene methyl isotopologs (light dashed lines).

The first spectrum in Figure 6a was recorded shortly after the end of the induction period (when BPE conversion was just 33 %). It represents a mixture of toluene- α - d_0 and - d_1 (Figure 6b). H/D exchange in the BPE methylene group prior to C-O bond cleavage was not detected (Scheme 4). We infer that toluene- α - d_1 is a direct result of the reaction of adsorbed D with adsorbed benzyl- α - d_0 (formed by C-O bond cleavage of BPE), eq 2, rather than a product of H/D exchange in the benzylic position of BPE prior to aryl ether cleavage.

$$PhCH2* + D* \leftrightarrows PhCH2D + 2*$$
 (2)

Figure 6a shows that the number of peaks in the toluene methyl region changes over time, reflecting the increasing extent of methyl deuteration. After 53 min, the 13 C singlet for toluene- d_0 was no longer visible; the resonances correspond to a mixture of toluene αd_1 , $-d_2$, and $-d_3$ (Figure 6b). The peaks in the methyl region continued to evolve after the maximum production of toluene was reached, ca. 100 min after the onset of BPE conversion (Figure 6b-c). This finding demonstrates that H/D exchange also occurs independent of C-O bond cleavage. Indeed, H/D exchange was observed when toluene- α - 13 C itself was heated at 175 °C in 2-PrOH with 50 bar D₂ in the presence of Ni/ γ -Al₂O₃, Figure S12. In that experiment, the final centroid location for the methyl resonances, 20.3 ppm, indicates a D content of 44 at% (by linear interpolation of the chemical shifts for toluene- α - d_0 and $-d_1$). This composition matches the fraction of exchangeable D (43 at%).

After BPE conversion was complete, the final centroid location for the toluene methyl resonances (20.1 ppm) is close to the chemical shift of toluene- α - d_2 , Figure 6c. The overall D content in the methyl group (63 at%, estimated by linear interpolation of the chemical shifts for toluene- α - d_1 and $-d_2$) resembles the fraction of exchangeable D (57 at%) in the reaction mixture (0.52 mmol 2-PrOD and 0.20 mmol H₂). The pseudo-first-order fit to the kinetic profile for the appearance of deuterated toluene from BPE in 2-PrOD under 50 bar H₂ yielded k_3 = (0.046 ± 0.006) s⁻¹ g_{cat}⁻¹ at 175 °C, Figure 6c. A slightly smaller value, k_3 = (.021 ± 0.006) s⁻¹ g_{cat}⁻¹, was measured for the reaction of toluene in 2-PrOH with 50 bar D₂ (corresponding to a similar total exchangeable D fraction, 43 at%), Figure S12.

Catalyst Activation. A pronounced induction period is evident in the kinetic profile for BPE hydrogenolysis in Figure 3. Its duration (ca. 41 min at 150 °C, estimated by extrapolating a first-order curvefit of the post-induction period kinetic profile to 100 % conversion) was reproducible in duplicate runs at the same temperature. At 135 °C or below, the induction period was prohibitively long. Attempts to follow the reaction at such temperatures using the same reactant and catalyst loadings resulted in no discernable BPE conversion even after *ca.* 15 h. At 160 and

170 °C, the induction period was shortened to ca. 23 and 15 min, respectively, Figure 4a. These observations suggest that activation of the Ni/γ -Al₂O₃ catalyst is slow under the reaction conditions.

Origin of the Extended Induction Period. The observed induction period is consistent with the reported kinetics of H_2 reduction of Ni/NiO materials, including those involving oxide monolayers⁵³ and bilayers,⁵⁴ as well as core/shell⁵⁵ structures. For example, removal of the oxide shell in MgAl₂O₄-supported Ni/NiO core/shell nanoparticles (3.2 nm) was reported to occur in the range 140-180 °C.⁵⁶ The reaction starts at the outermost NiO-covered surface, and occurs without the formation of intermediate oxide phases.⁵⁷⁻⁵⁸

In this study, the only Ni-containing phase visible in the powder XRD pattern of the air-exposed catalyst is Ni(0), with a mean nanoparticle diameter of ca. 14 nm (Figure S13). Variable-temperature EPR spectra, recorded in air between -170 and 20 °C, are also consistent with Ni(0). At the lower temperatures, the EPR resonance is dramatically broadened and shifted to lower fields (Figure 7). This behavior is characteristic of superparamagnetic Ni(0) nanoparticles.³⁷ EPR spectra of the air-exposed catalyst were also recorded in flowing H₂. The spectrum acquired at 20 °C was unchanged, but the EPR signal intensity increased slightly when the temperature was ramped to 170 °C, held for 30 min, then returned to room temperature, Figure S14. This change is consistent with reduction of an EPR-silent⁵⁹ surface oxide layer, causing the amount of EPR-active Ni(0) to increase.

XPS measurements were performed with 10.5 wt% Ni/ γ -Al₂O₃ to increase sensitivity. They confirm the presence of a minor NiO component associated with the air-exposed Ni nanoparticles, figure S15 and Table S2. HAADF-STEM imaging with EDX suggests that the NiO is present as a surface layer (Figure S16). The presence of a surface oxide was further verified by temperature-programmed reduction (TPR) of an air-exposed sample (Figure S17). The H₂ consumption corresponds to reduction of ca. 6 % of total Ni, in agreement with the H₂ consumption expected for reduction of a oxide monolayer (ca. 7%, Table S1).

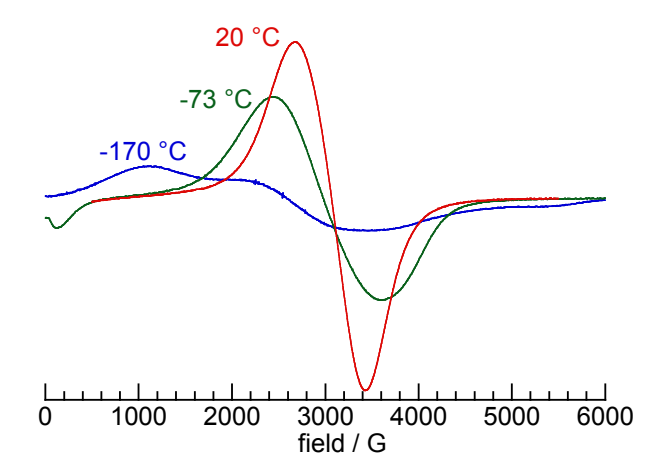


Figure 7. Variable-temperature EPR spectra of air-exposed Ni/ γ -Al₂O₃ (2 wt% Ni, ca. 14 nm average diameter nanoparticles).

Unlike Ni(0), NiO is an ineffective catalyst for hydrogenation and hydrogenolysis. 61 In this study, the reaction temperatures (150-175 °C) are too low to cause reduction of NiO nanoparticles (> 200 °C), 62 but they are consistent with reduction of a superficial oxide formed on Ni(0) nanoparticles exposed to O₂ at room

temperature. $^{26\text{-}28}$ The as-prepared Ni/ γ -Al₂O₃ catalyst was typically stored in air at room temperature for several days prior to use. The barrier for catalyst activation was estimated from the reciprocal of the induction time, τ . The Arrhenius plot gives a barrier of (72 ± 13) kJ mol $^{\text{-}1}$, Figure 8. Although literature values for NiO reduction are highly dependent on the reaction conditions, kinetically-controlled values fall in the range 65-98 kJ mol $^{\text{-}1}$. 57

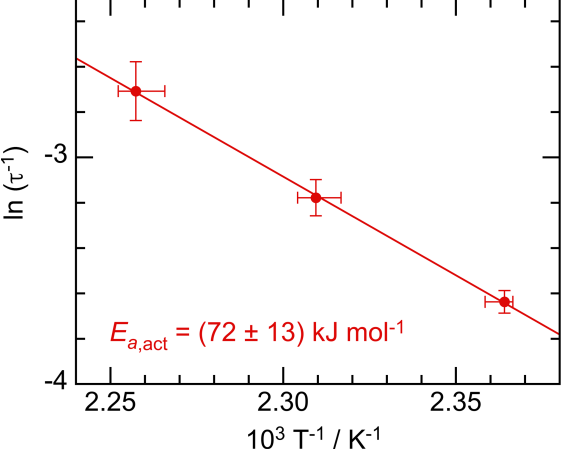


Figure 8. Arrhenius plot for the activation of air-exposed Ni/γ-Al₂O₃ by H₂ in 2-PrOH (red), based on the reciprocal of the duration of the induction period (τ) in BPE hydrogenolysis. The temperature error bars represent the thermal variability during the induction period, ca. 5 °C (estimated using 2-PrOH chemical shifts). The uncertainty in E_{a,act} reflects error propagation in the Arrhenius equation, ⁴⁷ not the error in the linear fit parameters.

Long induction periods have been reported for H_2 reduction of oxide-covered Ni surfaces. ^{57-58, 63-65} The H_2 sticking coefficient is low, ⁶⁶ however, adsorption of water on the oxidized Ni surface is strongly exothermic (-170 to -117 kJ mol⁻¹, depending on coverage). ⁶⁷ H_2 activation on oxygen vacancies ^{65, 68} can occur only after dehydration of the hydroxyl-terminated surface. ^{57, 69-70} Heterolytic dissociation of H_2 at a vacancy site produces adjacent

[NiH] and [NiOH] sites. When the hydride migrates (as a proton) to a neighboring oxygen, a second hydroxyl group is formed and a Ni(II) ion is reduced to Ni(0). Reduction is strongly autocatalytic, because Ni(0) activates H_2 much more readily than NiO. ⁵⁷⁻⁵⁸

Finally, when a reduced Ni/ γ -Al₂O₃ catalyst was stored under an inert atmosphere to avoid surface oxidation, then used in hydrogenolysis of BPE at 150 °C, the reaction commenced almost immediately, Figure S18.

Reaction Network for BPE Hydrogenolysis Catalyzed by Ni(0) Nanoparticles. A Langmuir-Hinshelwood mechanism for the primary reaction is shown in eq 3-7, where *indicates an unoccupied site on the Ni surface.

$$H_2 + 2^* \leftrightarrows 2H^* \tag{3}$$

$$PhCH_2OPh + * \leftrightarrows PhCH_2OPh^*$$
 (4)

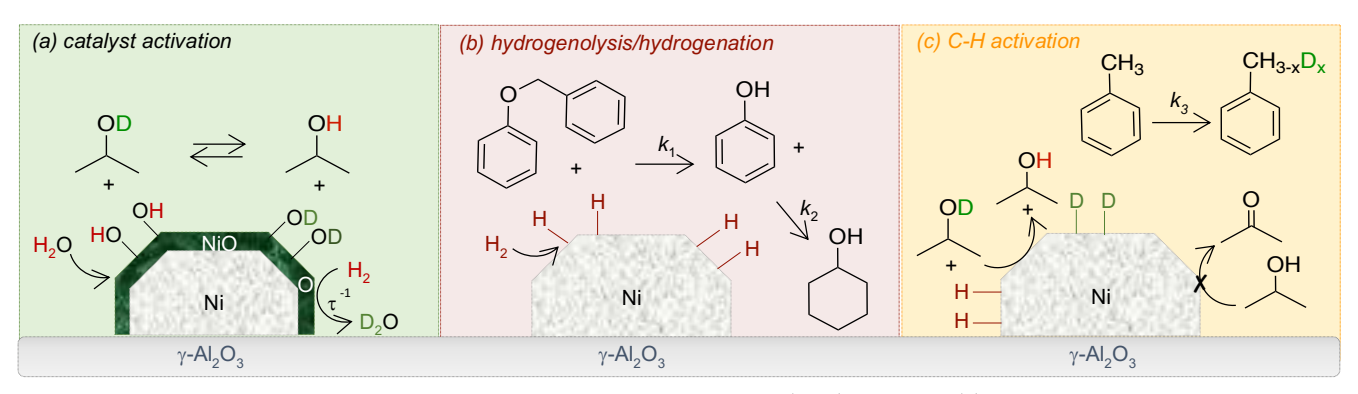
$$PhCH2OPh* + * \rightarrow PhCH2* + PhO*$$
 (5)

$$PhCH2* + H* + PhCH3* + *$$
 (6)

$$PhO^* + H^* \leftrightarrows PhOH^* + {}^* \tag{7}$$

C-O bond cleavage precedes aromatic hydrogenation, and is rate-determining. Adsorption of BPE is likely to require more than one site, but the first-order kinetic behavior suggests that the surface coverage of BPE is low. The weak dependence of the rate on $P(H_2)$ implies that H_2 and BPE do not compete directly for the same adsorption sites.

The 2-PrOH solvent does not supply adsorbed H under the reaction conditions, but its hydroxyl group does undergo rapid $\mathrm{Ni}(0)$ -catalyzed exchange with adsorbed H/D. This reaction makes the solvent the primary determinant of the isotopic composition of the adsorbed reducing equivalents. Both of the primary hydrogenolysis products, toluene and phenol, undergo subsequent reactions. Phenol is slowly hydrogenated to cyclohexanol, although subsequent dehydration of cyclohexanol was not observed. While toluene is not readily hydrogenated, $\mathrm{Ni}(0)$ catalyzes facile H/D exchange in its methyl group. The principal reactions are depicted in Scheme 5.



Scheme 5. Reaction network for catalytic hydrogenolysis of benzyl phenyl ether (BPE), depicting (a) Ni/γ -Al₂O₃ activation by reduction of the native surface (hydr)oxide, and H/D exchange with the 2-propanol solvent; (b) hydrogenolysis of BPE and subsequent hydrogenation of phenol; and (c) H/D exchange in the solvent and toluene.

CONCLUSIONS

Operando MAS-NMR spectroscopy provides detailed kinetic and mechanistic information about dynamic networks of reactions such as those that occur during hydrogenolysis of lignin and lignin model compounds catalyzed by supported metal catalysts in solution and in the presence of $H_{2(g)}$. Significant amounts of the solvent, as well as some solutes, are present in the vapor phase under these reaction conditions, but can be quantified by simple integration of their NMR signals. Temperature-sensitive solvent chemical shifts serve as an internal thermometer. Fortuitously, the

prolonged induction period caused by catalyst activation, as well as its abrupt end, facilitated the collection of high-quality isothermal kinetic data for BPE hydrogenolysis. Benzylic C-O bond cleavage is faster than $\rm H/D$ exchange in toluene, which in turn is faster than phenol hydrogenation.

Efforts are currently underway to examine the kinetics and mechanisms of reductive cleavage of other biomass model compounds, as well as whole lignin/biomass, extending the *operando* MAS-NMR technique to higher temperatures and pressures, and to examine variations in mechanism that arise due to the nature of the metal catalyst.

EXPERIMENTAL METHODS

Chemicals. The following were purchased from commercial suppliers and used as-received: toluene-α-¹³C and phenol-1-¹³C (98 %, 99 atom % ¹³C, Cambridge Isotopes), MnO₂ (≥ 99 %, Reagent Plus, Sigma-Aldrich), K₂CO₃ (99.7 %, Certified ACS, Fisher), 2-PrOH (anhydrous, 99.5 %, Sigma-Aldrich), 2-propanol- d_1 (99 %, 98 atom % D, Sigma-Aldrich), 2-propanol- d_8 (99 %, 99.5 atom % D, Sigma-Aldrich), D₂ (99.995 %, 99.96 atom % D, Sigma-Aldrich), Ni(NO₃)₂•6H₂O (98.5 %, Sigma-Aldrich), Br₂ (99.5 %, Merck), CH₂Cl₂, (CH₃)₂CO, ethyl acetate, and hexanes (all 99.9 %, Certified ACS), silica gel (230-400 Mesh, Fisher), γ-Al₂O₃ (≥ 97 %, pore volume: 0.40 mL/g, B.E.T. surface area 185 m²/g, Strem), hydrochloric acid (36.5 wt%, ACS grade, VWR), nitric acid (68 wt%, ACS grade, EMD-Millipore), H₂ (UHP grade, 99.999 %, Oxarc), and N₂O (9.99 vol% in He, Praxair).

Synthesis of $^{13}\text{C-Labelled Benzyl Phenyl Ether (BPE)}. \, ^{13}\text{C-labelled}$ benzyl bromide was prepared following a modified literature procedure. 71 Toluene- α - ^{13}C (100 mg, 1.07 mmol) was stirred with MnO $_2$ (93 mg, 1.07 mmol) and Br $_2$ (60 μL , 1.17 mmol) in CH $_2\text{Cl}_2$ (10 mL) for 1 h in a round-bottom flask (100 mL) until the solution became colorless. The mixture was filtered using a fritted glass Buchner funnel, then the benzyl bromide was purified on a silica column (elution with 5 % ethyl acetate in hexanes). Yield 145 mg, 80 %.

¹³C-labelled benzyl phenyl ether (BPE) was synthesized from the labeled benzyl bromide and phenol-1-¹³C using a modified literature procedure.⁷² A 100 mL round-bottom flask equipped with a magnetic stir bar and a condenser was charged with benzyl bromide (145 mg), phenol (100 mg), K₂CO₃ (180 mg) and (CH₃)₂CO (10 mL). The mixture was refluxed for 4 h until benzyl bromide consumption was complete according to TLC. After cooling to room temperature, the reaction mixture was filtered, and the product was purified by elution from a silica column with hexanes. ¹H and ¹³C spectra were recorded on a Varian Unity Inova 500 MHz spectrometer. Chemical shifts were referenced using solvent peaks as internal standards. ¹H NMR (500 MHz, DMSO-*d*₆): δ 5.10 (d, 2H), 7.00-7.02 (m, 2H), 7.28-7.39 (m, 7H). ¹³C NMR (125 MHz, DMSO-*d*₆): δ 69.03, 158.29 (¹³C-labeled positions only, Figure S19). Yield 130 mg, 66 %.

Synthesis and Characterization of Ni/ γ -Al₂O₃. The catalyst was prepared via incipient wetness impregnation, by stirring γ -Al₂O₃ (0.980 g) with an aqueous solution of Ni(NO₃)₂•6H₂O (62.3 mg in 0.400 mL deionized water). The solid was dried in an oven at 75 °C for 4 h, then calcined in air at 850 °C for 5 h, to give a material containing 1.9 wt% Ni (measured by ICP-AES). The metal is fully dispersed as Ni(II) ions in a pseudo-spinel structure according to

powder XRD (Figure S13). Reduction at 850 °C for 2 h in flowing 5% $\rm H_2/N_2$ (H5N, Airgas, 99.98 %) resulted in partial (ca. 55 %, based on $\rm H_2$ uptake) extrusion of Ni(0). According to $\rm H_2$ chemisorption, the nanoparticles have an average diameter of ca. 14 nm. The dispersion is 7 %, based on the total nickel content of the material.

Prior to the temperature-programmed reduction experiment, a sample of this H_2 -reduced catalyst (250 mg, ca. 2 wt% Ni) was exposed to air for 6 d at room temperature (Figure S17). To increase sensitivity in XPS measurements, a similar material containing 10.5 wt% Ni was prepared. Details of catalyst characterization by XPS, powder XRD, chemisorption, and HAADF-STEM/EDX mapping are presented in the Supporting Information.

In situ EPR Spectroscopy. EPR spectra were acquired on a Bruker Elexsys 580 spectrometer equipped with a SHQE resonator and a Bruker continuous flow liquid nitrogen cryostat (ER4131VT). The microwave frequency was typically 9.34 GHz with a power of 0.2 mW. The field was swept from 0 to 8000 G in 84 s and modulated at a frequency of 100 kHz with 0.5 G amplitude. A time constant of 20 ms was employed.

Operando MAS-NMR Spectroscopy. Magic-angle-spinning (MAS) NMR experiments were performed on an Agilent-Varian VNMRS NMR spectrometer equipped with an 11.7 T magnet, operating at 125.7747 MHz for the ¹³C channel and 500.1822 MHz for the ¹H channel. A 5-mm home-built magic-angle spinning (MAS) double resonance HX probe with a custom Pd–coated coil was used to maximize sample magnetic homogeneity. Calibration of the spectrometer temperature setting was performed by acquiring ²⁰⁷Pb NMR spectra of Pb(NO₃)₂.³⁵⁻³⁶

In direct polarization (DP) 13 C MAS-NMR experiments, a 35 kHz 1 H decoupling field was employed, with an acquisition time of 300 ms. The 13 C spectral width was 50 kHz, and 15,000 data points were acquired per transient, using a relaxation delay of 60 s to ensure quantitative analysis. At 25 $^{\circ}$ C, the T_{1} values for the methylene and 1-phenolate 13 C resonances of BPE, measured by saturation recovery experiments, are 4.4 and 15.3 s, respectively. For 1 H MAS-NMR experiments, spectra were collected by averaging 16 scans, with an acquisition time of 1 s and a relaxation delay of 10 s.

In a typical high T/P experiment, a customized³² 5 mm ZrO₂ rotor was loaded with BPE (2.0 mg, 0.011 mmol), Ni/ γ -Al₂O₃ (10 mg, 2 wt% Ni) and 2-PrOH (40 μ L), then pressurized with 50 bar H₂ (0.16 mmol) at room temperature. The total internal pressure at each temperature was estimated by summing the estimated partial pressures of H₂ and 2-propanol, calculated for a headspace volume that includes the volume of 2-PrOH liquid that vaporized. The MAS rate was 5 kHz. The first spectrum was collected when the probe reached its set temperature, typically 10-15 min after heating of the rotor commenced. Each transient spectrum was acquired by averaging 8 or 16 scans. ¹³C chemical shifts were referenced to TMS using adamantane as a secondary standard (37.48 ppm).⁷³

Batch Reactor Kinetics. BPE hydrogenolysis was conducted in a 25 mL stirred microreactor (Parr 4590) equipped with a sampling port. The reactor was charged with 2-PrOH (10 mL), BPE (0.54 mmol, 100 mg), Ni/ γ -Al₂O₃ (ca. 2 wt%, 500 mg), H₂ (50 bar), and *n*-decane (0.054 mmol, 10.5 μ L) as internal standard. The reactor was stirred at 300 rpm and heated to 150 °C (requiring a heating time of ca. 10 min for the temperature to stabilize). Aliquots (0.25 mL) were removed at timed intervals for analysis on a Shimadzu

GC-2010 gas chromatograph coupled to a Shimadzu GCMS-QP2010 mass spectrometer. The former instrument is equipped with a 30 m \times 0.25 mm Agilent DB-1 column with a dimethylpolysiloxane stationary phase (0.25 μ m).

Kinetic analyses. Kinetic profiles for conversion of BPE and production of toluene and phenol were analyzed by non-linear least-squares curvefitting using KaleidaGraph (Synergy Software). Concentrations of all species were normalized using the initial concentration of BPE.

ASSOCIATED CONTENT

Supporting Information

Supporting Information is available free of charge on the ACS Publications website.

Details of catalyst characterization; additional EPR, ¹³C and ¹H NMR spectra of standards and reaction mixtures; identification of deuterated toluene isotopologs by NMR and GC-MS; additional kinetic curvefits; (file type, PDF).

AUTHOR INFORMATION

Corresponding Author

* Correspondence to: sscott@ucsb.edu.

Funding Sources

The authors acknowledge funding from the U.S. National Science Foundation (CBET-1512228 and CBET-1604095). A.C. thanks UC Santa Barbara's Mellichamp Academic Initiative in Sustainability for partial fellowship support. L.Q. was supported during some of the writing of this manuscript by the Ames Laboratory (operated for the U.S. Department of Energy by Iowa State University under Contract No. DE-AC02-07CH11358). Ex situ NMR experiments made use of facilities provided by the MRSEC Program of the National Science Foundation (DMR-1121053). EPR and high temperature/pressure MAS-NMR experiments were conducted at PNNL's Environmental Molecular Sciences Laboratory, a DOE Office of Science User Facility sponsored by the Office of Biological and Environmental Research. PNNL is operated by Battelle for the DOE under Contract DE-AC05-76RL01830.

ACKNOWLEDGMENTS

We are grateful to Sarah Burton and Jesse Sears for their assistance in NMR instrument setup.

REFERENCES

- (1) Sievers, C.; Noda, Y.; Qi, L.; Albuquerque, E. M.; Rioux, R. M.; Scott, S. L. Phenomena Affecting Catalytic Reactions at Solid–Liquid Interfaces. *ACS Catal.* **2016**, *6*, 8286.
- (2) Ragauskas, A. J.; Beckham, G. T.; Biddy, M. J.; Chandra, R.; Chen, F.; Davis, M. F.; Davison, B. H.; Dixon, R. A.; Gilna, P.; Keller, M.; Langan, P.; Naskar, A. K.; Saddler, J. N.; Tschaplinski, T. J.; Tuskan, G. A.; Wyman, C. E. Lignin Valorization: Improving Lignin Processing in the Biorefinery. *Science* **2014**, *344*.
- (3) Tuck, C. O.; Pérez, E.; Horváth, I. T.; Sheldon, R. A.; Poliakoff, M. Valorization of Biomass: Deriving More Value from Waste. *Science* **2012**, *337*, 695.
- (4) Zakzeski, J.; Bruijnincx, P. C. A.; Jongerius, A. L.; Weckhuysen, B. M. The Catalytic Valorization of Lignin for the Production of Renewable Chemicals. *Chem. Rev.* **2010**, *110*, 3552.

- (5) Calvo-Flores, F. G.; Dobado, J. A. Lignin as Renewable Raw Material. *ChemSusChem* **2010**, *3*, 1227.
- (6) Azadi, P.; Inderwildi, O. R.; Farnood, R.; King, D. A. Liquid Fuels, Hydrogen and Chemicals from Lignin: A Critical Review. *Renew. Sust. Energ. Rev.* **2013**, *21*, 506.
- (7) Kandanarachchi, P. H.; Autrey, T.; Franz, J. A. Model Compound Studies of the β-O-4 Linkage in Lignin: Absolute Rate Expressions for β-Scission of Phenoxyl Radical from 1-Phenyl-2-phenoxyethanol-1-yl Radical. *J. Org. Chem* **2002**, *67*, 7937.
- (8) Parthasarathi, R.; Romero, R. A.; Redondo, A.; Gnanakaran, S. Theoretical Study of the Remarkably Diverse Linkages in Lignin. *J. Phys. Chem. Lett.* **2011**, *2*, 2660.
- (9) Beste, A.; Buchanan, A. C. Role of Carbon–Carbon Phenyl Migration in the Pyrolysis Mechanism of β -O-4 Lignin Model Compounds: Phenethyl Phenyl Ether and α -Hydroxy Phenethyl Phenyl Ether. *J. Phys. Chem.* **A 2012**, *116*, 12242.
- (10) Lankau, T.; Yu, C.-H. Intermediate Oxiranes in the Base-Catalyzed Depolymerisation of Lignin. *Green Chem.* **2016**, *18*, 1590.
- (11) Lu, J.; Wang, M.; Zhang, \dot{X} .; Heyden, A.; Wang, F. β -O-4 Bond Cleavage Mechanism for Lignin Model Compounds over Pd Catalysts Identified by Combination of First-Principles Calculations and Experiments. *ACS Catal.* **2016**, *6*, 5589.
- (12) Li, Q.; López, N. Chirality, Rigidity, and Conjugation: A First-Principles Study of the Key Molecular Aspects of Lignin Depolymerization on Ni-Based Catalysts. *ACS Catal* **2018**, 4230.
- (13) Bernt, C. M.; Bottari, G.; Barrett, J. A.; Scott, S. L.; Barta, K.; Ford, P. C. Mapping Reactivities of Aromatic Models with a Lignin Disassembly Catalyst. Steps Toward Controlling Product Selectivity. *Catal. Sci. Tech.* **2016**, *6*, 2984.
- (14) Kim, S.; Chmely, S. C.; Nimlos, M. R.; Bomble, Y. J.; Foust, T. D.; Paton, R. S.; Beckham, G. T. Computational Study of Bond Dissociation Enthalpies for a Large Range of Native and Modified Lignins. *J. Phys. Chem. Lett.* **2011**, *2*, 2846.
- (15) Froass, P. M.; Ragauskas, A. J.; Jiang, J.-E. Chemical Structure of Residual Lignin from Kraft Pulp. *J. Wood Chem. Technol.* **1996**, *16*, 347.
- (16) Tobisu, M.; Chatani, N. Catalytic Hydrogenolysis of C-O Bonds in Aryl Ethers. *ChemCatChem* **2011**, *3*, 1410.
- (17) Samant, B. S.; Kabalka, G. W. Hydrogenolysis-Hydrogenation of Aryl Ethers: Selectivity Pattern. *Chem. Commun.* **2012**, *48*, 8658.
- (18) Kelley, P.; Lin, S.; Edouard, G.; Day, M. W.; Agapie, T. Nickel-Mediated Hydrogenolysis of C–O Bonds of Aryl Ethers: What Is the Source of the Hydrogen? *J. Am. Chem. Soc.* **2012**, *134*, 5480.
- (19) Zaheer, M.; Kempe, R. Catalytic Hydrogenolysis of Aryl Ethers: A Key Step in Lignin Valorization to Valuable Chemicals. *ACS Catal.* **2015**, *5*, 1675.
- (20) Sun, Z.; Fridrich, B.; de Santi, A.; Elangovan, S.; Barta, K. Bright Side of Lignin Depolymerization: Toward New Platform Chemicals. *Chem. Rev.* **2018**, *118*, 614.
- (21) Schutyser, W.; Renders, T.; Van den Bosch, S.; Koelewijn, S. F.; Beckham, G. T.; Sels, B. F. Chemicals from Lignin: an Interplay of Lignocellulose Fractionation, Depolymerisation, and Upgrading. *Chem. Soc. Rev.* **2018**, *47*, 852.
- (22) Song, Q.; Wang, F.; Cai, J.; Wang, Y.; Zhang, J.; Yu, W.; Xu, J. Lignin Depolymerization (LDP) in Alcohol over Nickel-Based Catalysts via a Fragmentation-Hydrogenolysis Process. *Energy Environ. Sci.* **2013**, *6*, 994.
- (23) Zhang, X.; Chen, X.; Jin, S.; Peng, Z.; Liang, C. Ni/Al_2O_3 Catalysts Derived from Layered Double Hydroxide and Their Applications in Hydrodeoxygenation of Anisole. *ChemistrySelect***2016**, *1*, 577.
- (24) Gómez-Monedero, B.; Ruiz, M. P.; Bimbela, F.; Faria, J. Selective Hydrogenolysis of α-O-4, β-O-4, 4-O-5 CO Bonds of Lignin-

- Model Compounds and Lignin-Containing Stillage Derived from Cellulosic Bioethanol Processing. *Appl. Catal.*, A **2017**, 541, 60.
- (25) Cui, X.; Yuan, H.; Junge, K.; Topf, C.; Beller, M.; Shi, F. A Stable and Practical Nickel Catalyst for the Hydrogenolysis of C-O Bonds. *Green Chem.* **2017**, *19*, 305.
- (26) Payne, B. P.; Grosvenor, A. P.; Biesinger, M. C.; Kobe, B. A.; McIntyre, N. S. Structure and Growth of Oxides on Polycrystalline Nickel Surfaces. *Surf. Interface Anal.* **2007**, *39*, 582.
- (27) Song, P.; Wen, D.; Guo, Z. X.; Korakianitis, T. Oxidation Investigation of Nickel Nanoparticles. *Phys. Chem. Chem. Phys.* **2008**, *10*, 5057.
- (28) D'Addato, S.; Grillo, V.; Altieri, S.; Tondi, R.; Valeri, S.; Frabboni, S. Structure and Stability of Nickel/Nickel Oxide Core-Shell Nanoparticles. *J. Phys. Condens. Matter* **2011**, *23*, 175003.
- (29) Gómez, S.; Torres, C.; García Fierro, J. L.; Apesteguía, C. R.; Reyes, P. Hydrogenation of Nitrobenzene on Au/ZrO₂ Catalysts. *J. Chil. Chem. Soc.* **2012**, *57*, 1194.
- (30) Gu, S.; Wunder, S.; Lu, Y.; Ballauff, M.; Fenger, R.; Rademann, K.; Jaquet, B.; Zaccone, A. Kinetic Analysis of the Catalytic Reduction of 4-Nitrophenol by Metallic Nanoparticles. *J. Phys. Chem. C* **2014**, *118*, 18618.
- (31) Konuspaev, S. R.; Zhanbekov, K. N.; Kul'Kova, N. V.; Murzin, D. Y. Kinetics of 4 Tert butylphenol Hydrogenation Over Rhodium. *Chem. Eng. Technol.* **1997**, *20*, 144.
- (32) Walter, E. D.; Qi, L.; Chamas, A.; Mehta, H. S.; Sears, J. A.; Scott, S. L.; Hoyt, D. W. Operando MAS NMR Reaction Studies at High Temperatures and Pressures. *J. Phys. Chem.* C 2018, *122*, 8209.
- (33) Chamas, A.; Qi, L.; Mehta, H. S.; Sears, J. A.; Scott, S. L.; Walter, E. D.; Hoyt, D. W. High Temperature/Pressure MAS-NMR for the Study of Dynamic Processes in Mixed Phase Systems. *Magn. Reson. Imaging* **2019**, *56*, 37.
- (34) True, N. S., Gas Phase Applications of NMR Spectroscopy. In Encyclopedia of Spectroscopy and Spectrometry, 2nd ed.; Academic Press: Oxford, 2010; pp 749.
- (35) Bielecki, A.; Burum, D. P. Temperature Dependence of ²⁰⁷Pb MAS Spectra of Solid Lead Nitrate. An Accurate, Sensitive Thermometer for Variable-temperature MAS. *J. Magn. Reson., Ser. A* **1995**, *116*, 215.
- (36) Langer, B.; Schnell, I.; Spiess, H. W.; Grimmer, A.-R. Temperature Calibration under Ultrafast MAS Conditions. *J. Magn. Reson.* **1999**, *138*, 182.
- (37) Sharma, V. K.; Baiker, A. Superparamagnetic Effects in the Ferromagnetic Resonance of Silica Supported Nickel Particles. *J. Chem. Phys.* **1981**, *75*, 5596.
- (38) Kong, L.; Li, G.; Jin, L.; Hu, H. Effects of the Oxygen Substituent on the Pyrolysis of Phenyl Ethers on a Fixed-Bed Reactor. *J. Anal. Appl. Pyrolysis* **2015**, *115*, 362.
- (39) Luo, Y.-R., Comprehensive Handbook of Chemical Bond Energies. CRC Press: 2007; p 325.
- (40) He, J.; Zhao, C.; Lercher, J. A. Ni-Catalyzed Cleavage of Aryl Ethers in the Aqueous Phase. *J. Am. Chem. Soc.* **2012**, *134*, 20768.
- (41) Krüger, M. B.; Selle, C.; Heller, D.; Baumann, W. Determination of Gas Concentrations in Liquids by Nuclear Magnetic Resonance: Hydrogen in Organic Solvents. *J. Chem. Eng. Data* **2012**, *57*, 1737.
- (42) Limbach, H.-H.; Pery, T.; Rothermel, N.; Chaudret, B.; Gutmann, T.; Buntkowsky, G. Gas Phase ¹H NMR Studies and Kinetic Modeling of Dihydrogen Isotope Equilibration Catalyzed by Ru-Nanoparticles under Normal Conditions: Dissociative vs. Associative Exchange. *Phys. Chem. Chem. Phys.* **2018**, *20*, 10697.
- (43) Jaatinen, S.; Touronen, J.; Karinen, R.; Uusi-Kyyny, P.; Alopaeus, V. Hydrogen Solubility in Furfural and 2-Propanol: Experiments and Modeling. *J. Chem. Thermodyn.* **2017**, *112*, 1.
- (44) Espenson, J. H., Chemical Kinetics and Reaction Mechanisms. McGraw-Hill: New York, 2002.

- (45) Qi, S.-C.; Zhang, L.; Kudo, S.; Norinaga, K.; Hayashi, J.-i. Theoretical Study on Hydrogenolytic Cleavage of Intermonomer Linkages in Lignin. *J. Phys. Chem. A* **2017**, *121*, 2868.
- (46) Kang, M.; DeWilde, J. F.; Bhan, A. Kinetics and Mechanism of Alcohol Dehydration on γ -Al₂O₃: Effects of Carbon Chain Length and Substitution. *ACS Catal.* **2015**, *5*, 602.
- (47) Steigel, A.; Sauer, J.; Kleier, D. A.; Binsch, G. Nitrogen Analogs of Cycloheptatrienes and Norcaradienes. Nuclear Magnetic Resonance Study of their Thermodynamic and Kinetic Properties. *J. Am. Chem. Soc.* **1972**, *94*, 2770.
- (48) Vjunov, A.; Hu, M. Y.; Feng, J.; Camaioni, D. M.; Mei, D.; Hu, J. Z.; Zhao, C.; Lercher, J. A. Following Solid-Acid-Catalyzed Reactions by MAS NMR Spectroscopy in Liquid Phase—Zeolite-Catalyzed Conversion of Cyclohexanol in Water. *Angew. Chem. Int. Ed.* **2014**, *53*, 479.
- (49) Capponi, M.; Gut, I. G.; Hellrung, B.; Persy, G.; Wirz, J. Ketonization Equilibria of Phenol in Aqueous Solution. *Can. J. Chem.* **1999**, *77*, 605.
- (50) Mamaladze, L. M.; Gudkov, B. S.; Kiperman, S. L. Mechanism of Catalytic Hydrogenation of Toluene on Nickel Catalyst. *Bull. Acad. Sci. USSR, Div. Chem. Sci.* **1974**, *23*, 2512.
- (51) Alshehri, F.; Weinert, H. M.; Jackson, S. D. Hydrogenation of Alkylaromatics over Rh/Silica. *React. Kinet., Mech. Catal.* **2017**, *122*, 699.
- (52) Shin, E.-J.; Keane, M. A. Gas-Phase Hydrogenation/Hydrogenolysis of Phenol over Supported Nickel Catalysts. *Ind. Eng. Chem. Res.* **2000**, *39*, 883.
- (53) Vonk, V.; Khorshidi, N.; Stierle, A. Structure and Oxidation Behavior of Nickel Nanoparticles Supported on YSZ(111). *J. Phys. Chem.* C2017, 121, 2798.
- (54) Allen, G. C.; Tucker, P. M.; Wild, R. K. Surface Oxidation of Nickel Metal as Studied by X-Ray Photoelectron Spectroscopy. *Oxid. Met.* **1978**, *13*, 223.
- (55) Rellinghaus, B.; Stappert, S.; Wassermann, E. F.; Sauer, H.; Spliethoff, B. The Effect of Oxidation on the Structure of Nickel Nanoparticles. *Eur. Phys. J.* **D2001**, *16*, 249.
- (56) Kehres, J.; Andreasen, J. W.; Fløystad, J. B.; Liu, H.; Molenbroek, A.; Jakobsen, J. G.; Chorkendorff, I.; Nielsen, J. H.; Høydalsvik, K.; Breiby, D. W.; Vegge, T. Reduction of a Ni/Spinel Catalyst for Methane Reforming. *J. Phys. Chem.* C2014, 119, 1424.
- (57) Richardson, J. T.; Scates, R.; Twigg, M. V. X-ray Diffraction Study of Nickel Oxide Reduction by Hydrogen. *Appl. Catal., A* **2003**, *246*, 137.
- (58) Rodriguez, J. A.; Hanson, J. C.; Frenkel, A. I.; Kim, J. Y.; Perez, M. Experimental and Theoretical Studies on the Reaction of H₂ with NiO: Role of O Vacancies and Mechanism for Oxide Reduction. *J. Am. Chem. Soc.* **2002**, *124*, 346.
- (59) Xu, S.; Walter, E. D.; Zhao, Z.; Hu, M. Y.; Han, X.; Hu, J. Z.; Bao, X. Dynamic Structural Changes of SiO₂ Supported Pt–Ni Bimetallic Catalysts over Redox Treatments Revealed by NMR and EPR. *J. Phys. Chem.* C2015, 119, 21219.
- (60) Alonso, F.; Riente, P.; Sirvent, J. A.; Yus, M. Nickel Nanoparticles in Hydrogen-Transfer Reductions: Characterisation and Nature of the Catalyst. *Appl. Catal., A* **2010**, *378*, 42.
- (61) Borgschulte, A.; Westerwaal, R. J.; Rector, J. H.; Dam, B.; Griessen, R. Hydrogen Sorption Mechanism of Oxidized Nickel Clusters. *Appl. Phys. Lett.* **2004**, *85*, 4884.
- (62) Salagre, P.; Fierro, J. L. G.; Medina, F.; Sueiras, J. E. Characterization of Nickel Species on Several γ-alumina Supported Nickel Samples. *J. Mol. Catal. A: Chem.* **1996**, *106*, 125.
- (63) Syed-Hassan, S. S. A.; Li, C.-Z. NiO Reduction with Hydrogen and Light Hydrocarbons: Contrast Between SiO₂-Supported and Unsupported NiO Nanoparticles. *Appl. Catal.*, *A* **2011**, *398*, 187.

- (64) Furstenau, R. P.; McDougall, G.; Langell, M. A. Initial Stages of Hydrogen Reduction of NiO(100). *Surf. Sci.* **1985**, *150*, 55.
- (65) Villarrubia, J. S.; Ho, W. Reaction of Hydrogen with Adsorbed Oxygen on Ni(110). *Surf. Sci.* **1984**, *144*, 370.
- (66) Hock, M.; Küppers, J. Interaction of Hydrogen and Oxygen at Ni(111) Surfaces. *Surf. Sci.* **1987**, *188*, 575.
- (67) Zhao, W.; Bajdich, M.; Carey, S.; Vojvodic, A.; Nørskov, J. K.; Campbell, C. T. Water Dissociative Adsorption on NiO(111): Energetics and Structure of the Hydroxylated Surface *ACS Catal.* **2016**, *6*, 7377.
- (68) Benton, A. F.; Emmett, P. H. The Reduction of Nickelous and Ferric Oxides by Hydrogen. *J. Am. Chem. Soc.* **1924**, *46*, 2728.
- (69) Xu, Q.; Cheah, S.; Zhao, Y. Initial Reduction of the NiO(100) Surface in Hydrogen. J. Chem. Phys. 2013, 139, 024704.

- (70) Chen, J. G.; Fischer, D. A.; Hardenbergh, J. H.; Hall, R. B. A Fluorescence-Yield Near-Edge Spectroscopy (FYNES) Investigation of the Reaction Kinetics of NiO/Ni(100) with Hydrogen. *Surf. Sci.* **1992**, *279*, 13.
- (71) Mathew, K. M.; Ravi, S.; Unny, V. K. P.; Sivaprasad, N. Microwave-Assisted Synthesis of (RS) Methyl-2-([2'-14C]4,6-dimethoxypyrimidin-2'-yloxy)-2-phenyl [1-14C]ethanoate. *J. Label. Compd. Radiopharm* **2006**, *49*, 699.
- (72) Wu, W.-B.; Huang, J.-M. Electrochemical Cleavage of Aryl Ethers Promoted by Sodium Borohydride. *J. Org. Chem* **2014**, *79*, 10189.
- (73) Morcombe, C. R.; Zilm, K. W. Chemical Shift Referencing in MAS Solid State NMR. *J. Magn. Reson.* **2003**, *162*, 479.

Table of Contents artwork

